energies

MDPI

Article

Shape Optimization of Heat Exchanger Fin Structures Using the Adjoint Method and Their Experimental Validation

Marco Fuchs *, Cagatay Necati Dagli and Stephan Kabelac

Institute of Thermodynamics, Leibniz University Hannover, An der Universität 1, 30823 Garbsen, Germany; dagli@ift.uni-hannover.de (C.N.D.); kabelac@ift.uni-hannover.de (S.K.)

* Correspondence: fuchs@ift.uni-hannover.de

Abstract: The freedom of additive manufacturing allows for the production of heat-transferring structures that are optimized in terms of heat transfer and pressure loss using various optimization methods. One question is whether the structural optimizations made can be reproduced by additive manufacturing and whether the adaptations can also be verified experimentally. In this article, adjoint optimization is used to optimize a reference structure and then examine the optimization results experimentally. For this purpose, optimizations are carried out on a 2D model as well as a 3D model. The material chosen for the 3D optimization is stainless steel. Depending on the weighting pairing of heat transfer and pressure loss, the optimizations in 2D result in an increase in heat transfer of 15% compared to the initial reference structure with an almost constant pressure loss or a reduction in pressure loss of 13% with an almost constant heat transfer. The optimizations in 3D result in improvements in the heat transfer of a maximum of 3.5% at constant pressure loss or 9% lower pressure losses at constant heat transfer compared to the initial reference structure. The subsequent experimental investigation shows that the theoretical improvements in heat transfer can only be demonstrated to a limited extent, as the fine contour changes cannot yet be reproduced by additive manufacturing. However, the improvements in pressure loss can be demonstrated experimentally following a cross-section correction. It can therefore be stated that with increasing accuracy of the manufacturing process, the improvements in heat transfer can also be utilized.

Keywords: additive manufacturing; adjoint optimization; heat transferring structures; high temperature; experimental testing

Citation: Fuchs, M.; Dagli, C.N.; Kabelac, S. Shape Optimization of Heat Exchanger Fin Structures Using the Adjoint Method and Their Experimental Validation. *Energies* **2024**, *17*, 1246. https://doi.org/10.3390/en17051246

Academic Editor: Artur Blaszczuk

Received: 7 February 2024
Revised: 28 February 2024
Accepted: 1 March 2024
Published: 5 March 2024

1. Introduction

The elimination of many manufacturing restrictions through additive manufacturing opens up new possibilities for the optimization of heat-transferring structures. This is also accompanied by the practical application of various optimization techniques that can be used to further optimize and improve structures. The optimization methods for heat-transferring structures can basically be divided into three categories: size (parameter) optimization, shape optimization and topology optimization. This article focuses on the shape optimization of fins that can be used in compact heat exchangers, for example.

Size optimization is the most basic form of structural optimization. In this variant, the geometry of a heat-transferring structure is first clearly described by corresponding parameters, e.g., fin height, mesh size or web diameter. During the course of the optimization, these defined geometry parameters are varied in order to determine the optimum of a predefined target or cost function. The general shape of the structure remains unchanged; only its size varies.

The basics for size optimization are formed by numerical and/or experimental parameter variations of various structural parameters in order to determine the influence on heat transfer and pressure loss. As a result, correlations are usually created which map the influences through simple geometric relationships. The best-known examples are the geometry variations and

derived correlations for off-set strip fins, wavy fins or louvered fins. The design freedom of additive manufacturing further expands this parameter space and also adds new structures, the best-known representatives of which are so-called "lattice structures" and "minimal surface structures". Niknam et al. [1] provided an overview of various additively manufactured structures (fins, lattice structure and minimal surface) and the parameter variations carried out, in which the influence of parameter variation on heat transfer and pressure loss is investigated, for example by Liang et al. [2] on various lattice structures or Tang et al. [3] on so-called "minimal surface structures". The disadvantage of this method lies in the restriction to fixed geometry parameters, which means that a potential optimum is limited to the choice of geometry. Furthermore, the computational requirements of this method rise sharply with an increasing number of parameters, which is drastically increased by the degrees of freedom of additive manufacturing and the associated additional geometries. The possibilities of parameter optimization in the development of heat exchangers are thus largely exhausted or can no longer be carried out with reasonable effort, so other methods must be used to achieve further performance improvement.

In shape optimization, the entire shape of a previously defined geometry is changed. This can be done, for example, by approximating the shape using polynomials, as presented in Bacellar et al. [4] or Wenterodt [5], which are then modified using an optimization criterion. Other variants of shape optimization are the manual adjustment of the shape based on developed flow profiles, e.g., to reduce detachment areas. This method offers the advantage that further optimization can be achieved following size optimization, for example, by reducing areas that are unfavorable to the flow. However, this type of shape optimization requires all flow variables to be solved again after each design change, which also results in a considerable computational effort for increasingly complex geometries or polynomial approximations with corresponding parameters. Shape optimization, on the other hand, can be accelerated by applying the adjoint approach, in which only the sensitivity of the change of the boundary to the flow variable is calculated.

Vidya [6] performed optimizations on pin fins, focusing on a single pin fin in 3D and on a pin fin array in 2D. Through optimization, an increase in heat transfer and a reduction in pressure loss can be achieved. Wang et al. [7] used a 3D adjoint approach to optimize the fins of a heat exchanger to reduce the drag. Czerwinski et al. [8] used the adjoint approach to optimize the fin geometry of a heat sink for electronics cooling to increase the performance. Kametani et al. [9] carried out an optimization and experimental investigation of cylinders in 3D using the adjoint approach, whereby they obtained the turbulent variables from a direct numerical simulation for the specific optimization case. This procedure allows for completely new structural shapes to be determined, although the basic design or arrangement of the bodies (the topology) is retained. This approach was extended to V-shaped oblique wavy fins by Kametani et al. [10], and they tested different weight factors and their impact on heat transfer and pressure loss.

However, it is important to note that a high-quality mesh must be maintained during the optimization, particularly in the case of automated shaping methods, in order to obtain a physically plausible result. Furthermore, the choice of the turbulence model and its implementation in an adjoint optimization has a major influence on the calculation results, especially if a large number of design iterations are carried out, as Kühl, Müller and Rung [11] show. It is therefore advisable to carry out a complete remeshing with high mesh quality following the optimization in order to check the optimization results accordingly. Ideally, an experimental investigation should also be carried out in order to check the reproducibility of the optimizations made by the manufacturing process.

This is where this article comes in. The structures developed are mainly used in compact heat exchangers, which are used for high-temperature fuel cell and electrolysis systems as well as Power-to-X ("P2X")-systems.

An example of such a heat exchanger is shown in Figure 1. This plate-and-fin heat exchanger consists of several layers through which the hot and cold fluid flows in counterflow. Inside, the heat exchanger is equipped with fin-like structures that are optimized for the additive manufacturing process.

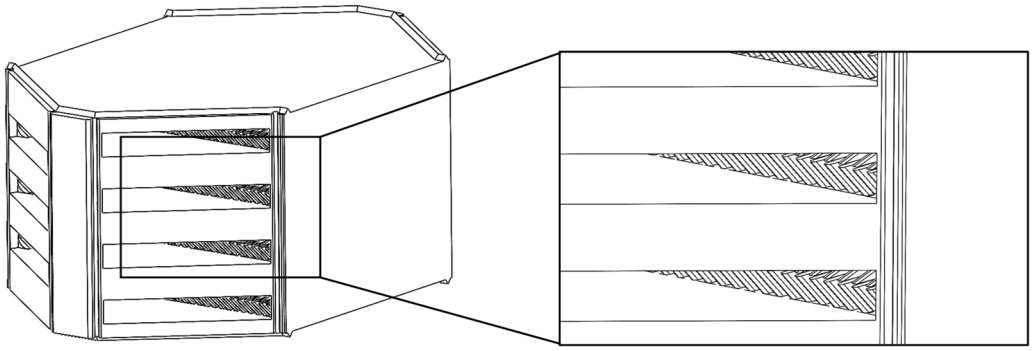

Figure 1. Example of an additive-manufactured heat exchanger with internal fins.

These heat exchangers must be designed in such a way that low-pressure losses are achieved with high efficiency and a high degree of compactness, as stated in Li et al. [12], for example, in SOFC systems. This means that the heat exchangers are only operated in the laminar flow range, as is often the case with compact heat exchangers [13]. However, this results in small Nusselt numbers due to the low turbulence and rapid decay of turbulent effects. The increase in performance must therefore be achieved in particular through thin thermal boundary layers, which, however, also causes correspondingly thin hydrodynamic boundary layers, resulting in increased wall shear stresses and thus increased frictional pressure losses. The aim must therefore be to develop structures in which unfavourable areas for heat transfer are reduced in order to reduce the pressure loss and at the same time, expand areas that have a positive effect on heat transfer. For this task, therefore, shape optimization of fin-like structures is to be carried out, whereby the initial design point is a manual optimization, which was carried out under heat transfer aspects. This optimization is further refined in 2D and 3D by means of the adjoint optimization. By varying the weights for heat transfer and pressure loss, a Pareto front is created so that different optimized geometries are ultimately available depending on the application focus. Two of the optimized structures are then tested experimentally to ensure that the optimization measures can be reproduced in production.

2. Materials and Methods

The initial design for the optimizations presented in this paper is based on a parameter variation of different fin parameters (fin height, fin spacing, fin length and fin longitudinal displacement), which are presented in Fuchs et al. [14]. The different fin parameters are evaluated on the basis of their entropy production number, and a parameter combination that has the lowest entropy generation is selected [15]. Based on this fin geometry, various optimizations for high heat transfer and low-pressure loss have been carried out by adjusting the fin shape to the corresponding thermal and hydrodynamic boundary layer. Furthermore, a reduction in detachment areas and a reduction in excessive flow acceleration at sudden changes in cross-section has been achieved, which was validated in [16]. This process is shown in Figure 2 on the left side and in the center part.

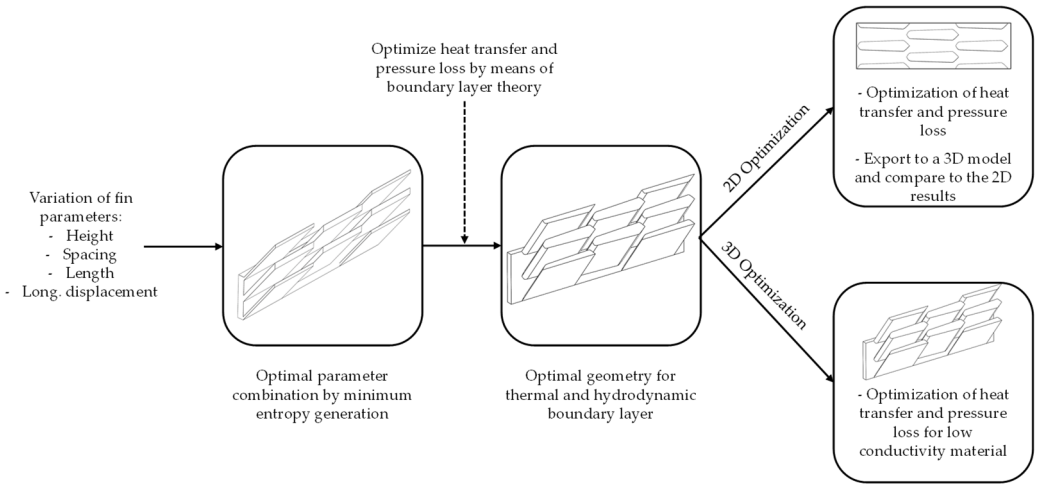

Figure 2. Left: development process towards the reference structure in [14–16]. **Right**: two optimization directions presented in this article.

Based on this reference structure, further optimizations with a focus on heat transfer and pressure loss will be carried out in both 2D and 3D in this article using the Adjoint Method; see also Figure 2 on the right. The 2D optimization is used to check the extent to which an optimization can also be transferred to three dimensions, as a 2D optimization could be carried out much faster. For this purpose, the 2D optimization aims to improve the heat transfer at a constant pressure loss and the resulting shape is then transferred to 3D, using both aluminum ($\lambda_{Al} = 155$ W/mK) and stainless steel ($\lambda_{Al} = 16$ W/mK) as materials.

Furthermore, 3D optimizations are also carried out in order to improve the reference structure further by taking into account the heat conduction within the fin structure. The focus here is also on increasing the heat transfer while at the same time reducing or keeping the pressure loss constant. The 3D optimization is only carried out with stainless steel.

The initial models, or the reference structure, for the 2D and 3D optimization are shown in Figure 3 as 3D and 2D models.

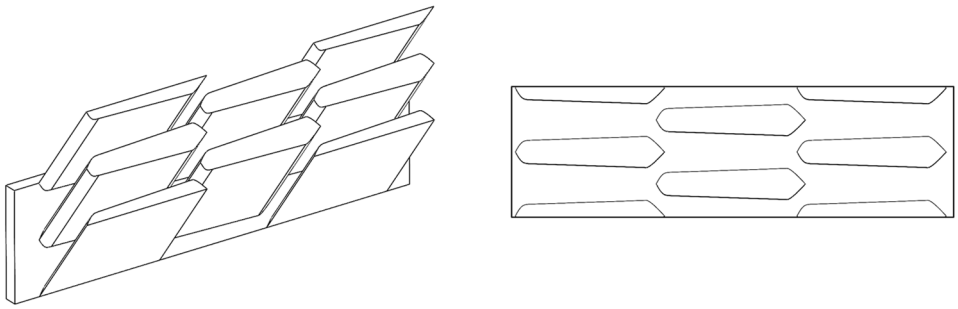

Figure 3. Model of the reference structure in 3D and 2D.

2.1. Simulation Settings

Ansys Fluent 2021 R2 [17] and Ansys Meshing 2021 software are used for the numerical flow calculations of the reference geometry, the subsequent adjoint optimization and remeshing. The CAD model is created using SolidWorks 2021 [18], SpaceClaim 2021 and DesignModeler 2021 [19].

The calculation is time-stationary and the flow is assumed to be incompressible. The pressure-based solver "Coupled" is used.

The flow in the structures is macroscopically in the laminar range. However, the turbulence model k-ω SST [20] is still used in order to be able to correctly capture a possible turbulent transition as well as any local turbulence that may occur. A comparison of the

calculation results of the k-ω SST model with a laminar model in Table 1 shows an average deviation of 0.039% for the pressure loss and 0.086 K for the outlet temperature at Reynolds numbers of 89, 306 and 498. The results of the k-ω SST model are therefore classified as valid.

Table 1. Comparison of the laminar and the k-ω SST calculation for the reference structure.

Re [-]	**89**	**306**	**498**
$T_{\text{out,lam}} - T_{\text{out,SST}}$ $[K]$	0.0038	−0.0159	0.2033
$\frac{\Delta p_{\text{lam}}}{\Delta p_{\text{SST}}} \times 100$ [%]	0.018	0.042	−0.058

Second-order upwind schemes are used as discretization schemes for the conservation equations, and first-order upwind schemes are used for the turbulence discretization in order to increase the calculation accuracy.

2.2. Adjoint Optimization

As mentioned at the beginning, the optimization of heat-transferring structures for a high heat transfer and a low-pressure loss is subject to the problem of a large number of available geometric degrees of freedom. This is further exacerbated by the rectified interaction of the two objective functions, as a high heat transfer is usually accompanied by an increased pressure loss. This makes the optimization of heat-transferring structures based on parameter variations very computationally intensive and therefore inefficient, especially in the context of additive manufacturing.

This increased computational effort can be countered by the adjoint approach. The method calculates the sensitivities of an objective function as a function of the available design parameters and is therefore clearly superior to other "direct" methods in terms of computing power [21].

The adjoint approach can be divided into the "discrete" and the "continuous adjoint approach". In this paper, the "discrete adjoint approach" is used through the use of Ansys Fluent and is therefore briefly introduced based on the descriptions by Gauger [22], as this provides a good understanding of the underlying ideas. For the exact implementation in ANSYS Fluent, please refer to the Fluent Theory Guide [23].

A cost function Z to be optimized can be influenced by the design variable R (e.g., the physical boundary) as well as by the flow variables (S), so we have $Z = Z(R, S)$. Similarly, the equations for calculating the flow variables (G), such as pressure, velocity and temperature also change due to changes in the design variables and other flow variables (e.g., the change in the pressure field when the velocity field changes), therefore $G = G(R, S)$ applies. As these are conservation equations, we can put $G = 0$.

When $G = 0$, the optimization problem Z can be expressed using the Lagrange duality:

$$L = Z + \lambda^T G, \tag{1}$$

where λ^T denotes the Lagrangian Multiplier. The derivative of L according to the design variable R leads to the following expression:

$$\frac{dL}{dR} = \frac{\partial Z}{\partial R} + \frac{\partial Z}{\partial S}\frac{dS}{dR} + \lambda^T\left[\frac{\partial G}{\partial S}\frac{dS}{dR} + \frac{\partial G}{\partial R}\right] \tag{2}$$

and can be transformed to:

$$\frac{dL}{dR} = \left(\frac{\partial Z}{\partial R} + \lambda^T\frac{\partial G}{\partial R}\right) + \left[\left(\frac{\partial Z}{\partial S} + \lambda^T\frac{\partial G}{\partial S}\right)\frac{dS}{dR}\right]. \tag{3}$$

The calculation of λ^T is carried out using the following bracketed expression of the second term:

$$\left(\frac{\partial Z}{\partial S} + \lambda^T \frac{\partial G}{\partial S}\right) = 0 \rightarrow \frac{\partial Z}{\partial S} = -\lambda^T \frac{\partial G}{\partial S} \tag{4}$$

and is referred to as an "adjoint equation". This means that the computing time-intensive calculation of the flow variables can be dispensed, and the gradient of the variable L to be optimized only depends on the design variables R:

$$\frac{dL}{dR} = \left(\frac{\partial Z}{\partial R} + \lambda^T \frac{\partial G}{\partial R}\right). \tag{5}$$

The result is the sensitivity of the optimization variable to a change in the design variable [24]; for example, if the mesh is moved in the x,y,z-direction.

If there is a multi-objective function, this can be expressed by individual objective functions in combinations with weights [6] as follows:

$$Z = \sum_{i=1}^{N} w_i Z_i(R, S). \tag{6}$$

By selecting the weights, the optimization can be directed towards the different target functions; for example, more in the direction of pressure loss or in the direction of heat transfer. A Pareto front can thus be created from different weights, each of which represents an optimum for heat transfer and pressure loss depending on the weights. It follows that this method also requires the selection of parameters, but the number is significantly lower than with the usual gradient-based parameter methods.

The consideration of turbulent variables during adjoint optimization is the subject of numerous studies [9,11,25], as they can have a considerable influence on the result depending on the flow condition. In this article, the k-ω SST model, which is not yet available as an adjoint variant in Fluent, is used. In Fluent, the turbulence variables are, therefore, kept constant when calculating the sensitivities. This means that no sensitivities of the turbulent variables are available for the change in the design variables. This principle is referred to as "frozen turbulence" [6]. The influence of this principle on the calculation result is, of course, highly dependent on the turbulence present, as [26] shows. In this article, the structures are operated in the (macroscopic) laminar flow region and transition region so that the turbulent quantities are orders of magnitude smaller than in the fully turbulent region. Therefore, the "frozen turbulence" assumption will be used in the following adjoint optimization.

Freeform Scale Factor or Step Size

After calculating the sensitivities, geometry changes can be determined based on the defined cost function values. After defining a desired cost function value change, Fluent calculates the new expected value. This value is multiplied by the so-called "freeform scale factor" (FFSF) (or step size) and results in a new value after adjusting the geometry. The freeform scale factor acts as a kind of amplification factor and leads to correspondingly stronger changes in geometry and stronger changes in the new cost function value. Following the corresponding geometry change, mesh morphing takes place in order to adapt the mesh accordingly.

However, this results in the problem that the choice of the optimum freeform scale factor is unknown. A value that is too small leads to very long calculation times, while a value that is too large causes the geometry to change too much and therefore, a potential optimum is not found. In addition, large FFSFs lead to strong mesh distortions, so sometimes, only a few design iterations are possible before remeshing becomes necessary. It is, therefore, necessary to start with an appropriate investigation of how sensitive the changes to the geometry affect the target variable. Once the geometry has been adjusted, the flow variables are iterated again, and the adjoint variables are calculated, resulting in

the sensitivities for the next design iteration. In this way, the optimum can be approached in a gradient-like manner with repeated runs. The strength of Adjoint Optimization is derived from this: instead of a large number of (manual) geometry changes and corresponding flow calculations, only the sensitivities are calculated.

2.3. Boundary Conditions for the Numerical Calculations and Optimization Region

The 2D and 3D structures presented in this article differ in boundary conditions (BC). Figure 4 shows the 2D initial structure with the corresponding boundary conditions. A constant velocity ($u_{in} = 2.7$ m/s) is selected at the inlet for the optimization; the inlet cross-section temperature is $T_{in} = 355.8$ K. Air is used as the fluid; the fluid properties are calculated as a function of temperature using polynomials in accordance with the VDI Heat Atlas [27]. A relative outlet pressure of 0 Pa is assumed at the outlet of the flow area, and an outflow area is modelled.

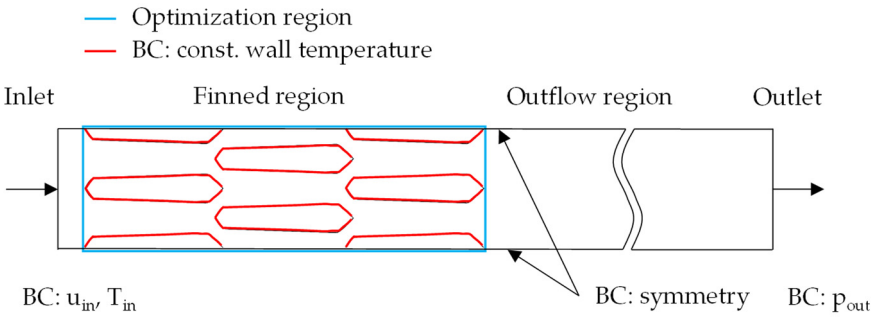

Figure 4. Calculation domain for the 2D optimization with boundary conditions and optimization region.

The choice of boundary conditions at the fins is more challenging. In reality, neither an exactly constant wall temperature nor a constant heat flux prevail in a fin cross-section. For example, there are typically significantly higher heat fluxes in the area of the stagnation point than in the area of the fin flank, so the assumption of constant heat flux for the entire fin wall would be less suitable. However, heat conduction within the fin (in the direction of flow) leads to a more uniform temperature, which is why the constant wall temperature of 550 K is ultimately chosen as the boundary condition.

The upper and lower areas are provided with symmetry conditions. The fin contour is only optimized in the area marked in blue so that the overall length of the structures remains unchanged.

The boundary conditions for the 3D optimization are shown in Figure 5. A constant velocity ($u_{\mathrm{in}} = 2.7$ m/s) and an inlet temperature of $T_{\mathrm{in}} = 355.8$ K are again specified at the inlet cross-section. The boundary condition "pressure outlet" (p_{out}) is specified at the outlet with a relative outlet pressure of 0 Pa, as for the 2D case.

In the 3D case, the finned structures are part of the side wall, and both are made of stainless steel, which ensures the separation between the hot and cold fluid in the later heat exchangers. If such a heat exchanger is now operated in counterflow, constant heat flux in the side wall can be assumed when a developed flow is present. As the 3D case is more or less a mini section of such a counterflow heat exchanger, a constant heat flux is set for the side wall. This also allows the formation of a realistic temperature profile within the fins, which is particularly important for materials with low thermal conductivity.

The opposite side is provided with a symmetry condition since only half a channel is simulated. Symmetrical boundary conditions are also set at the top and bottom. The front and rear sides of the wall are assumed to be adiabatic. The interface between fluid and solid (side wall and fins) is assumed to be coupled, i.e., a conjugate heat transfer problem.

The optimization area for the adjoint optimization is also limited to the fins in the 3D case, with the optimization box (area marked in blue) again extending from the front edge of the fins to the rear edge of the last row of fins and from the wall to the top edge of

the fins. As in the 2D case, this is intended to ensure a constant overall volume and thus prevent increased heat transfer from being achieved simply by using longer fins.

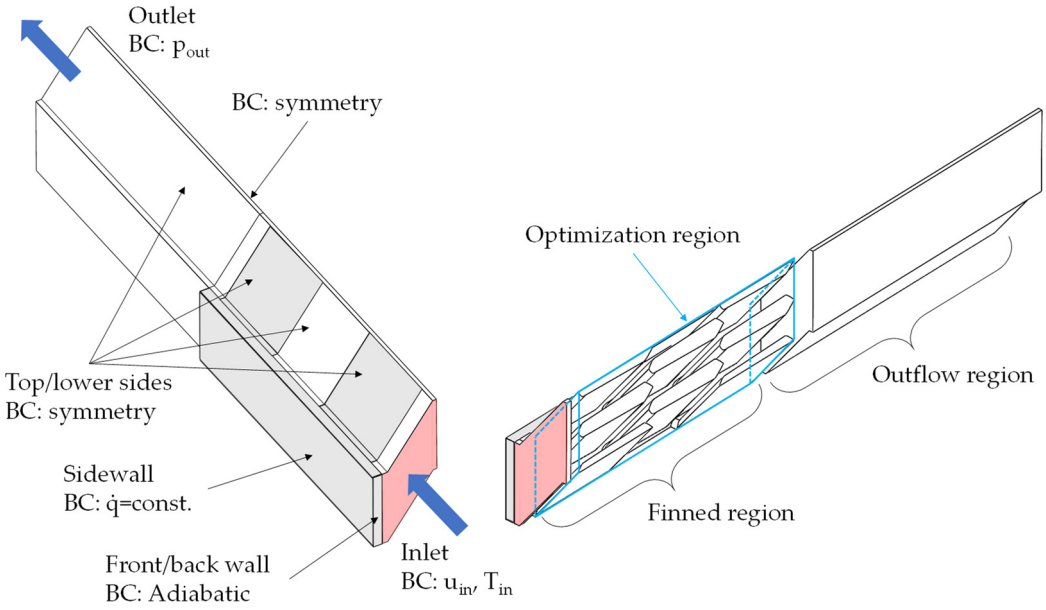

Figure 5. Calculation domain for the 3D Optimization with boundary conditions (red area: Inlet, grey area: part of the solid domain) and optimization region (blue lines).

2.4. Meshes for the 2D and 3D Optimization

The mesh used for 2D optimization is shown in Figure 6. The meshing with tetrahedra cells with an element size of 0.035 mm is based on the results of a mesh independence study, considering heat transfer and pressure loss, shown in Table 2.

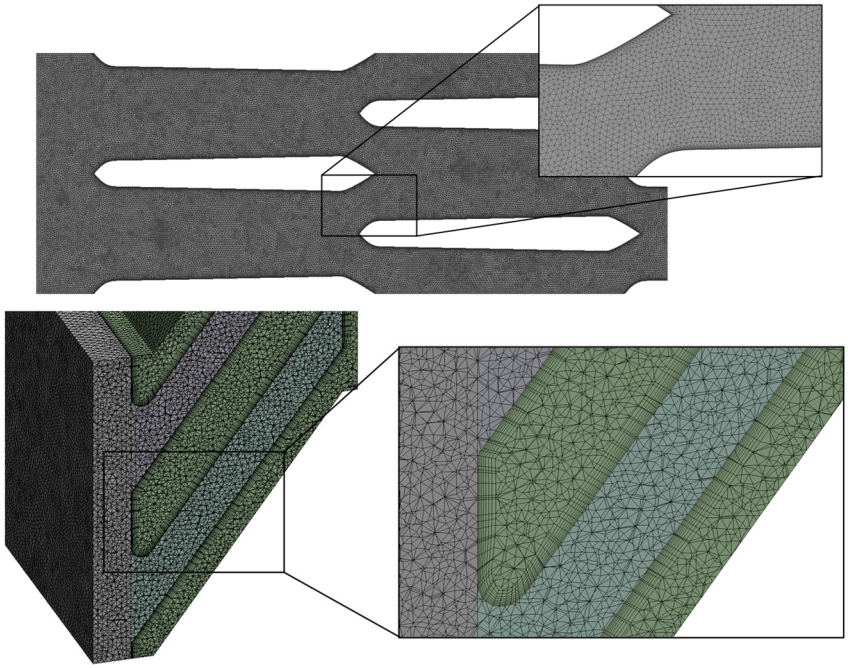

Figure 6. Top: Mesh for the 2D optimization and detail of the inflation layer. **Bottom**: Mesh for the 3D optimization and detail of the inflation layers (the green area indicates the fluid domain, the grey and the blue area the solid parts).

Table 2. Check for mesh independence for the reference mesh in 2D.

Variable	Mesh 1	Mesh 2	Mesh 3
No. of Elements in thou.	87	132	176
Temperature difference in K	42.516	42.518	42.520
Pressure loss in Pa	24.135	24.364	24.368

The boundary layers are resolved with 10 inflation layers at a growth rate of 20%. This fine resolution is necessary to achieve the highest possible minimum orthogonal quality of 0.5 to allow for a sufficient number of iterations during the optimization without excessive mesh distortion.

The mesh for the 3D optimization is shown at the bottom of Figure 6 and is significantly more complex than for the two-dimensional case. A very high orthogonal quality (minimum orthogonal quality of 0.17) should be achieved in order to allow a sufficient number of design iterations. The general element size is set at 0.08 mm; the boundary layer areas are provided with eight inflation layers at a 20% growth rate. The mesh independence checks in Table 3, as well as the investigations of the reference structure in Fuchs et al. [16], confirm the accuracy of the mesh.

Table 3. Check for mesh independence for the reference mesh in 3D.

Variable	Mesh 1	Mesh 2	Mesh 3
No. of Elements in Mio.	4.8	5.7	6.9
Temperature difference in K	42.91	42.944	42.948
Pressure loss in Pa	73.38	73.62	73.72

2.4.1. Mesh Morphing

The presented Adjoint Optimization calculates sensitivities for the corresponding observables, which are used to make changes to the geometry. These geometry changes, therefore, make it necessary to adapt the computational mesh in order to recalculate the sensitivities in the next design iteration. This is known as mesh morphing. This article uses a polynomial-based morphing approach from Fluent, as it modifies both the near-wall and the far-wall mesh and thus enables a more accurate solution. The large-scale mesh deformation is calculated using Bernstein polynomials, while the fine-scale mesh deformation is calculated using B-spline polynomials. For more detailed explanations, please refer to the Fluent Users Theory Guide [28].

2.4.2. Mesh Improvement

Mesh morphing inevitably leads to mesh distortion, which increases with increasing design iterations. The orthogonal quality and skewness deteriorate accordingly, which increases the inaccuracies in the results. Therefore, a mesh correction is required after a certain number of design iterations. This is done in two ways in this article. Firstly, the correction is carried out using a mesh improvement implemented in Fluent, in which cells with low orthogonal quality are split into several tetrahedra cells. This is particularly important for the 3D optimization, as a higher mesh distortion occurs after fewer iterations than in the 2D case. This automated mesh correction thus enables further design iterations.

The second mesh correction is carried out in the 2D case by means of a complete remeshing at the end of the calculations. For this purpose, the optimization is interrupted once the orthogonal quality is less than 0.1, and the resulting geometry is exported as a .stl-file. The structure is then remodelled in SolidWorks to be completely remeshed with the initial mesh settings specified above.

2.5. Determination of the Heat Transfer Coefficients

Different variables are used for the subsequent comparison of the optimizations and the general evaluation. These are the fraction of heat flow and logarithmic temperature difference, the Colburn j-factor and the Fanning f-factor.

The fraction of heat flow and logarithmic temperature difference are used to compare the changes in the heat transfer coefficient, the surface efficiency η_0 and the heat transferring surface $A_{\mathrm{ht,tot}}$ as a whole resulting from the optimizations, especially in the Pareto diagrams. The corresponding equation is:

$$\alpha \, A_{\mathrm{ht,tot}} \, \eta_0 = \frac{\dot{Q}}{\Delta T_{\log}}, \tag{7}$$

with

$$\Delta T_{\log} = \frac{(T_{\mathrm{f,in}} - T_{\mathrm{w,in}}) - (T_{\mathrm{f,out}} - T_{\mathrm{w,out}})}{\ln \frac{(T_{\mathrm{f,in}} - T_{\mathrm{w,in}})}{(T_{\mathrm{f,out}} - T_{\mathrm{w,out}})}} \tag{8}$$

as a logarithmic temperature difference for the case of constant heat flux density. The temperature differences between the wall and the fluid at the inlet and outlet are used for the evaluation.

The length-averaged temperatures at the contact line between the fluid and the wall directly in front and behind the fin structure are used for the wall temperatures. The fluid temperatures are used then at the same location in the form of the mass flow average temperatures. The heat flow is determined via an energy balance around the fluid $\dot{Q} = \dot{m} \, \overline{c_p} \, (T_{\mathrm{f,out}} - T_{\mathrm{f,in}})$. The specific isobaric heat capacity is calculated with the arithmetic mean temperature between inlet and outlet. Figure 7 shows the positions of the temperatures as well as the areas and lines for the evaluation.

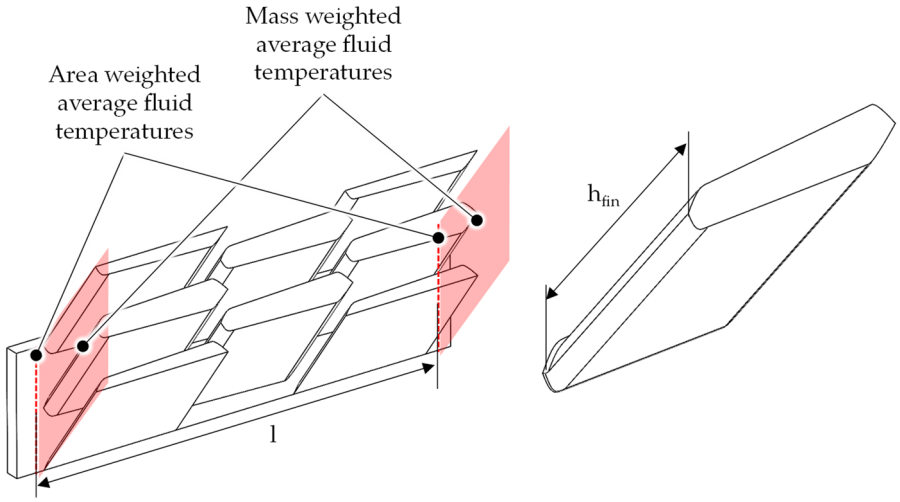

Figure 7. Left: Positions for the fluid and wall temperature evaluation. **Right**: fin height.

For further determination of the heat transfer coefficient α, the surface efficiency must be determined:

$$\eta_0 = 1 - \frac{A_{\mathrm{ht,fin}}}{A_{\mathrm{ht,tot}}}(1 - \eta_{\mathrm{fin}}) \tag{9}$$

with the fin efficiency for straight fins:

$$\eta_{\mathrm{fin}} = \frac{\tanh\left(\sqrt{\frac{\alpha \, P}{\lambda_{\mathrm{fin}} \, A*}} \, h\right)}{\sqrt{\frac{\alpha \, P}{\lambda_{\mathrm{fin}} \, A*}} \, h}. \tag{10}$$

The total heat transferring surface $A_{\mathrm{ht,tot}}$ in the considered area is made up of the base area and the fin *area* $A_{\mathrm{ht,fin}}$ minus the fin base area. The fin cross-section $A*$ and the fin perimeter P are determined on the basis of a single fin. Table 4 provides an overview of the geometric data of a single fin.

Table 4. Geometric data for the reference fin.

Fin Type	h_{fin} [mm]	A* [mm^2]	P [mm]
Reference fin	4.65	2.4	10.07

The Colburn j-factor can now be calculated using the following equation:

$$j = \frac{\alpha\, d_h}{\overline{\lambda}_f\, \mathrm{RePr}^{1/3}}. \tag{11}$$

whereas d_h denotes the hydraulic diameter and $\overline{\lambda_f}$ the thermal conductivity of the fluid. As with the heat capacity, the thermal conductivity is calculated at the average fluid temperature between the inlet and outlet. The hydraulic diameter is determined at the point of the narrowest flow cross-section, where the following equation applies $d_h = 4\frac{A_{c,f}\, l}{A_{ht,tot}}$. $A_{c,f}$ describes the minimum flow cross-section, $A_{ht,tot}$ the total heat transferring surface and l the length of the area $A_{ht,tot}$. This is also illustrated in Figure 7. The heat transfer coefficient can now be determined via a simple iterative procedure, such as the Newton method.

The Fanning f-factor, which can be determined directly from the pressure loss calculations, is used to evaluate the pressure loss as a dimensionless variable. It is determined using the following equation:

$$f = \Delta p \frac{d_h}{l}\frac{\rho}{2}\left(\frac{A_{c,f}}{\dot{m}}\right)^2. \tag{12}$$

The density is determined at the arithmetic mean temperature between the inlet and outlet. For the length l, the length of the calculation domain is used, as shown in Figure 7.

Finally, the Reynolds- number is defined as follows:

$$\mathrm{Re} = \frac{\dot{m}\, d_h}{A_{c,f}\, \overline{\eta_f}}. \tag{13}$$

The dynamic viscosity is calculated based on the arithmetic mean fluid temperature. The Colburn j-factors and the Fanning f-factors determined can now be used to derive correlations for the various structures. The correlations for calculating the j- and f-factors are power laws with adjustable parameters. The following approach is used for the j-factor:

$$j = C_j \mathrm{Re}^{n_j} \tag{14}$$

and for the f-factor:

$$\mathrm{f} = C_f \mathrm{Re}^{n_f} \tag{15}$$

The adjustable parameters C_j, n_j, C_f, n_f are determined using a simple regression method based on the results for all Reynolds numbers for each structure.

2.6. Test Rig

The test rig in which the additive-manufactured heat exchangers are tested is shown in Figure 8. The test rig provides two air flows that are heated to the desired temperature by electric heaters. The flow rate is controlled by two MassFlow controllers (type Bronkhorst F203AV and Bürkert type 8746). The inlet and outlet temperatures are measured using type K thermocouples with diameters of ø1 mm and ø0.5 mm, which are calibrated in advance. Two thermocouples are installed in each inlet and outlet port to determine a possible temperature gradient across the cross-section in the fluid in order to make any corrections to the structure of the mixing chamber. These mixing chambers are installed in front of the thermocouples at 40 mm intervals in order to supply the thermocouples with a more uniform temperature profile. As the measurements are carried out at up to 700 °C, the influence of radiation must also be taken into account [29]. For this purpose,

the surrounding temperature measurement areas are equipped with a heater so that the pipe wall temperature can be set accordingly, as shown in Figure 9.

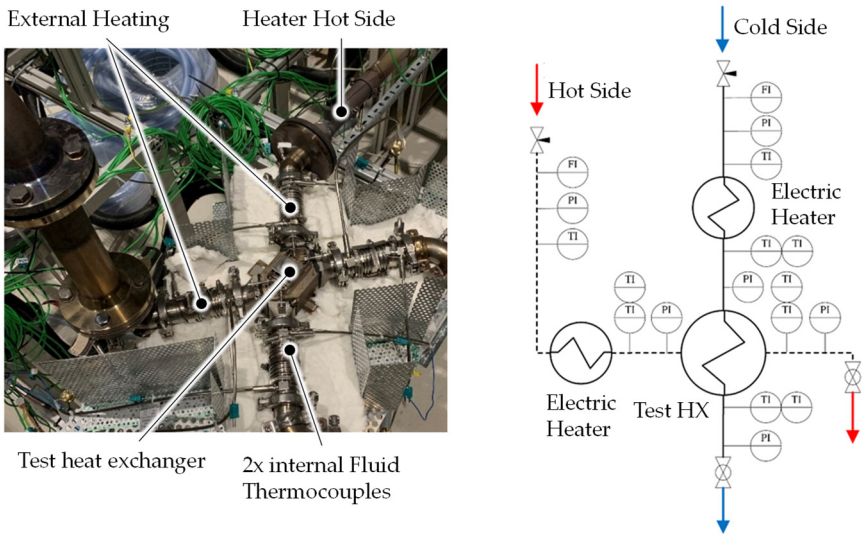

Figure 8. Left: position of the heat exchanger with inlet and outlet connections. **Right**: flow chart of the test rig.

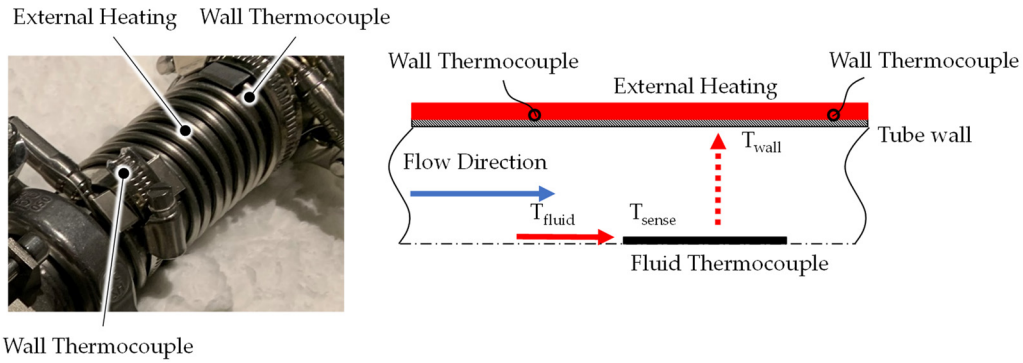

Figure 9. Left: Detail of the external heating for radiation compensation. **Right**: the principle of radiation compensation.

With this control, the temperature of the surrounding pipe wall is raised to 1–2 K below the measured fluid temperature, which drastically reduces the influence of heat radiation. The principle of this wall heating and the principle is shown in Figure 9. The pressure losses are measured using precision U-tube pressure gauges, as the measured pressure losses cover a wide range, thus ensuring consistent accuracy. Furthermore, the U-tube pressure gauges are not subject to drift, which makes it easy to compare the results. The measurement uncertainties are calculated using the "Guide to the expression of the uncertainty in measurements" (GUM) [30].

2.6.1. Test Heat Exchangers

The optimizations made are to be verified by means of experiments. For this purpose, two heat exchangers with optimized structures are manufactured. The external dimensions of the heat exchangers are identical; only the internal structures differ.

For the experimental validation, a structure with a focus on optimized heat transfer and another structure with a focus on reduced pressure loss is selected. The two heat exchangers are made of AISI 316L stainless steel. Figure 10 shows such a heat exchanger with connecting flanges and a layer with the internal structure. Each heat exchanger

consists of a total of 7 layers, alternating between a cold and hot layer (four cold and three hot). The heat exchangers are designed in a counterflow configuration.

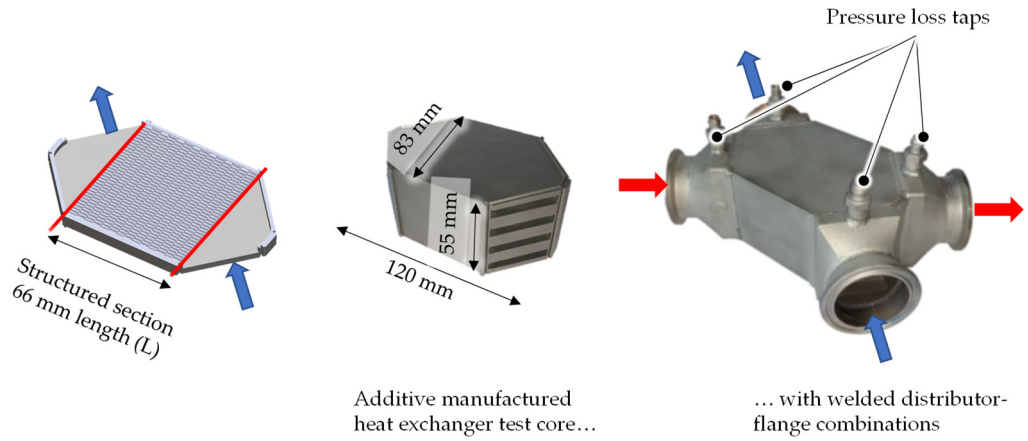

Figure 10. Left: one layer of the heat exchanger with a marked area for the fins, **middle**: 3D-printed heat exchanger core with external dimensions. **Right**: final heat exchanger with welded distributors and flanges. The blue and red arrows indicate the cold and hot fluid.

For the evaluation of the optimized structures, the heat transfer area, the flow cross-section area and the hydraulic diameter of a heat exchanger with the reference structure are used. This allows a better comparison of the results, as it is no longer possible to precisely determine the geometric variables (in particular the flow cross-section area) of the optimized variants. The geometric values for the evaluation are listed in Table 5.

Table 5. Geometric data for the evaluation.

Geometric Characteristics	Total Heat Transfer Area $A_{ht,tot}$ [m^2]	Fin Heat Transfer Area $A_{ht,fin}$ [m^2]	Flow Cross-Section Area $A_{c,f}$ [m^2]	Hydraulic Diameter d_h [m]
Value	0.1729	0.1545	7.642×10^{-4}	1.18×10^{-3}

For the investigations, the mass flows of the hot and cold fluid are varied between 0.1–0.5 kg/min. Furthermore, three temperature levels (h/c: 200/80 °C, 400/80 °C, 700/380 °C) are investigated in order to detect a possible radiation influence in addition to the convective heat transfer. This results in a Reynolds number range of 70–800, with both balanced and unbalanced flows being examined in order to investigate the performance of the structures over a wide range.

2.6.2. Evaluation Methodology of the Experimental Results

The Colburn j-factor and the Fanning f-factor are also to be determined from the experimental data. For the j-factor, a method from Fuchs et al. [16] is used. At first, the measured fluid inlet and outlet temperatures are used to determine the overall heat transfer coefficient for the different mass flow rates:

$$kA_{exp,i} = \frac{\dot{Q}_{cold,i}}{\Delta T_{log,i}} = \frac{\dot{m}_{c,i}\,\bar{c}_{p,c,i}\,(T_{c,out,i} - T_{c,in,i})}{ln\frac{(T_{h,in,i}-T_{c,out,i})-(T_{h,out,i}-T_{c,in,i})}{(T_{h,in,i}-T_{c,out,i})}}. \quad (16)$$

Second, a mathematical model (Fuchs et al. [31]) of the heat exchanger is used to calculate the theoretical overall heat transfer coefficients $kA_{th,i}$, by using approach functions for the j-factor (see Equation (14)). By varying the parameters $C_{j,exp}$ and $n_{j,exp}$ in the model

using a genetic algorithm, the error of the cost function s is minimized for all measuring points (mass flows); the following applies:

$$s = \min_{\vec{x}=(C_{j,exp},n_{j,exp})} \left(\sqrt{\frac{1}{N_{test}-1} \sum_{i=1}^{N_{test}} \left(1 - \frac{kA_{exp,i}}{kA_{th,i}\left(\vec{x}\right)} \right)^2} \right). \quad (17)$$

This procedure is necessary in order to eliminate the influence of axial heat conduction and heat transfer in the inlet and outlet distributors of the heat exchanger from the measurement results and to enable a direct comparison with the numerical data.

The overall pressure loss of the heat exchanger can be divided into pressure losses due to contraction and expansion at the in- and outlet of the distributor as well as the pressure loss due to friction in the finned section, which lead to:

$$\Delta p_{tot} = \Delta p_{con,Dist} + \Delta p_{fric,fin} + \Delta p_{ex,Dist}. \quad (18)$$

The evaluation of the pressure losses in the distributor is calculated with the following equation:

$$\Delta p_{ex/con,Dist} = \zeta_{ex,con,Dist} \frac{\rho}{2} u_{max}^2. \quad (19)$$

For the velocity u_{max}, the velocity in the smaller cross-section is chosen throughout. The determination of the loss coefficients $\zeta_{ex/con,Dist}$ is based on the diagrams according to Kays [32] for "multiple square tubes" for the Reynolds number Re_{max} and the respective flow area ratio.

The Fanning f-factor for the finned section f_{fin} is determined using the following equation:

$$f_{fin} = \Delta p_{fric,fin} \frac{d_h}{L} \frac{\overline{\rho}}{2} \left(\frac{A_{c,f}}{\dot{m}} \right)^2. \quad (20)$$

For the measurement, the length of the structured section L of the heat exchanger is used, please see Figure 10.

3. Results

3.1. Optimization in 2D and Transfer to 3D

First, the 2D structure is optimized on the basis of the reference structure. A FFSF of 15 is used for the optimization, as this represents the best compromise between shape change and mesh quality. This is kept constant for further design iterations.

The exact cost function FLUENT is using is not known; for the 2D multi-objective optimization the goal is to minimize the pressure loss and maximize the fluid outlet temperature, so the optimization objective is:

$$Z = \min f\left(w_{T_{out}},\ (1/T_{out}), w_{\Delta p}, \Delta p\right). \quad (21)$$

T_{out} is the mass-weighted average fluid temperature at the outlet and Δp the overall pressure loss of the entire fluid domain (refer to Figure 4).

The optimization can now be carried out using the determined FFSF. The weight factors are $w_{T_{out}} = 0.\overline{77}$ and $w_{\Delta p} = 0.\overline{22}$ to increase the heat transfer at a constant pressure loss; this structure is referred to as A27. The weights were obtained by a "try-and-error" method. The optimization is initially carried out for a Reynolds number of Re = 200. Figure 11 shows the contour plots of the velocity and temperature for different design iterations with the same weights and the same FFSF. This clearly shows that with increasing design iterations, the fin structures are increasingly drawn out in length and interlock with each other. Furthermore, a more pointed design of the stagnation points can be seen, which, in combination with the entanglement, leads to thin thermal boundary layers. The

analysis of the change in geometry also shows that the change in geometry slows down after 140 design iterations.

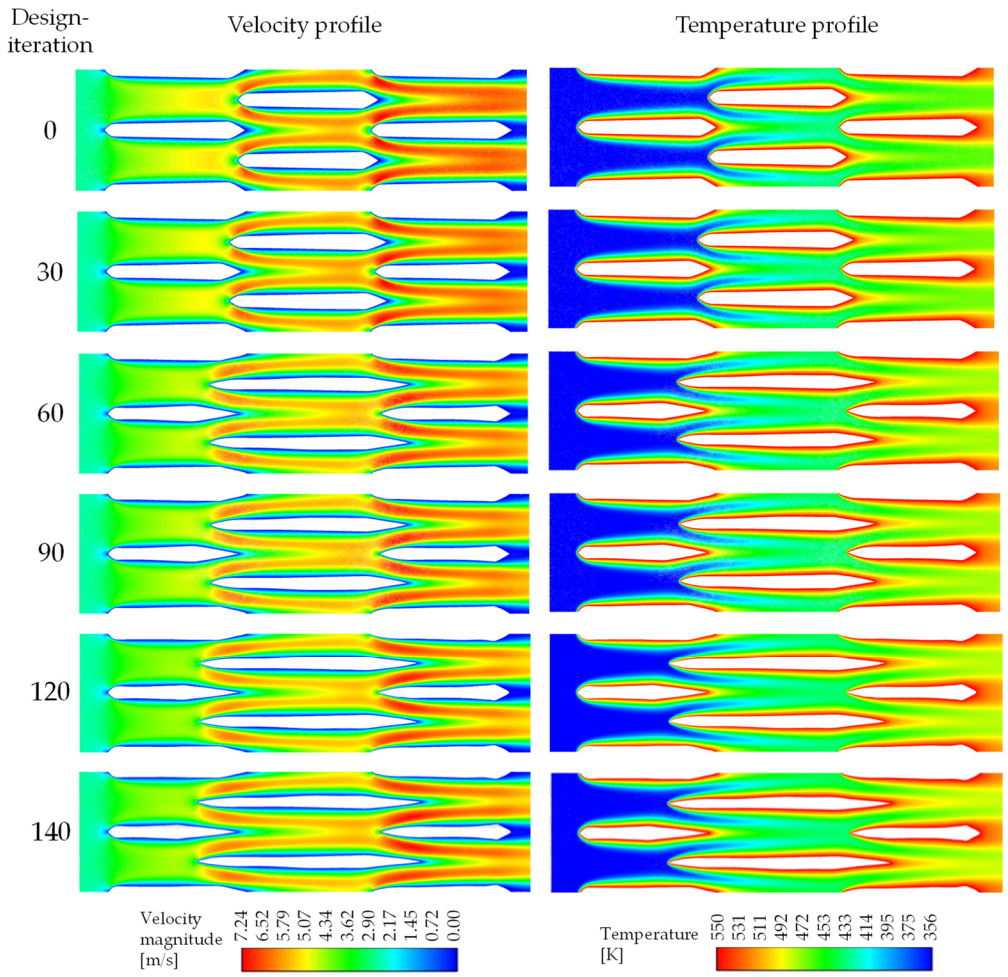

Figure 11. Velocity and temperature profile for different design iterations.

Furthermore, after 140 design iterations, a manufacturing limit is reached, particularly at the leading and trailing edge of the fin, as also stated in [33]. Figure 12 illustrates this case. Due to the limited diameter of the laser spot of ~50 µm, the leading and trailing edges of the fins cannot be resolved by the laser and, therefore, are not manufactured accurately. As a consequence, further optimization in this area would not make any sense since it would have no effect on the later experiments.

As a result, for 140 iterations, an increase in the heat transfer rate of 16.1% is achieved for A27, while the pressure loss decreases by 0.5%.

Based on the optimization with the designation A27, further optimizations are now carried out to reduce pressure loss. For the single objective optimization the objective function changes to $Z = \min f(w_{\Delta p}, \Delta p)$ with $w_{\Delta p} = 1$ and a FFSF of 15. In order to prevent this from happening simply by reducing the fin cross-section, any change in shape in the y-direction is suppressed. The reason for this is that the fin efficiency cannot be taken into account in 2D optimization. If an optimization is carried out with a focus on a lower pressure loss, there is a risk that the fins will be made thinner, which would drastically reduce the fin efficiency. Furthermore, the manufacturability limit would be undercut, especially in the inflow and outflow area of the fin, which would mean that the optimization could no longer be verified experimentally. A total of 17 design iterations are carried out. Figure 13 shows the fin shapes after design iterations 5, 11 and 17. These structures are referred to as B27, C27 and D27.

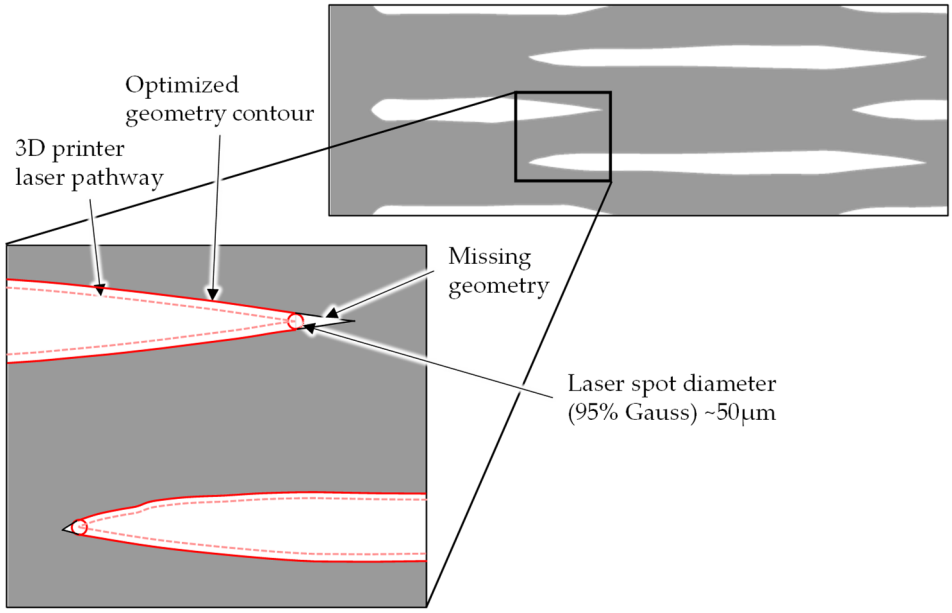

Figure 12. Detail of the design iteration 140 with the 3D printer laser pathway (dashed red line) and the missing geometry (black lines) at the leading and trailing edge of the fin.

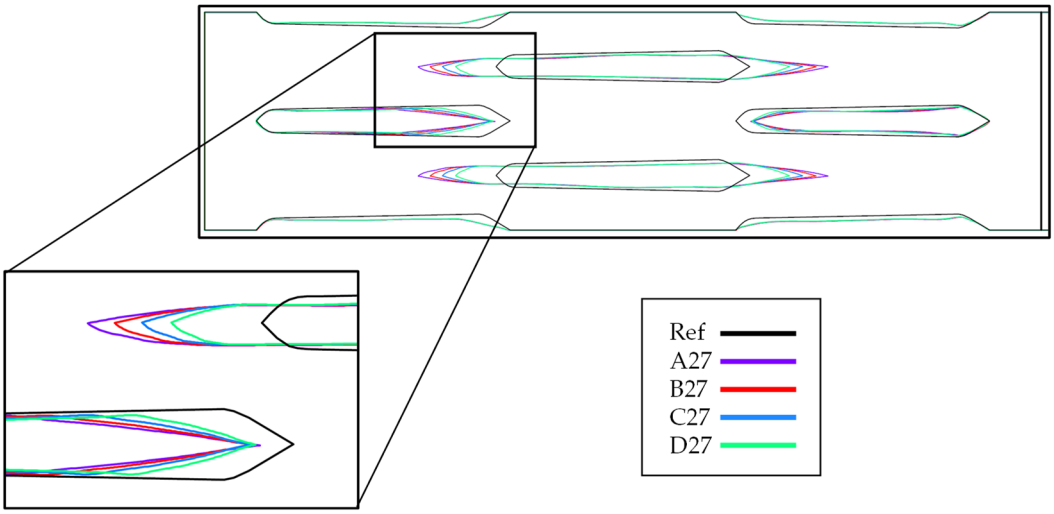

Figure 13. Geometry contours for the different pressure loss optimizations.

The figure shows that the fins become shorter as the number of iterations increases and the overlap decreases, which reduces the pressure losses, but at the same time the product of heat transfer coefficient and heat transfer area also decreases. As a result, a reduction in pressure loss of 14.3% and an increase in the "heat transfer*area" product of 3.7% is achieved for structure D27; see the 2D values in Figure 15.

In the next step, these shapes are converted into three dimensions in order to achieve better comparability, also taking into account the fin efficiency. For this purpose, the optimized 2D geometries are exported as .stl files, converted into a solid body and transferred into 3D, as indicated in Figure 14. The structures have an inclination angle of 37° to the vertical to enable additive manufacturing; the normal height is 2.8 mm. These 3D structures are then meshed and provided with boundary conditions in accordance with Figure 5. The calculations are performed with both aluminum and stainless steel to evaluate the influence of different materials.

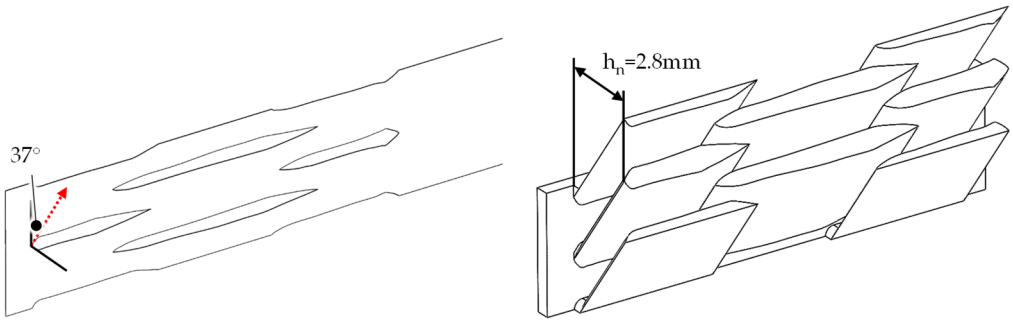

Figure 14. Left: 2D structure of A27 with direction for extrusion (red arrow). **Right**: extruded fins of A27 to a normal height of 2.8 mm.

For the 3D case, no improvement compared to the 3D-reference structure in heat transfer can be determined for the stainless-steel variant, which is between 91 and 95% of the reference structure, see Figure 15. As a result of the thin thermal boundary layer at the fin tip, there are high heat transfer coefficients, which only lead to low heat flux densities compared to the reference structure due to the smaller solid cross-section at the fin tip. This leads to a greater drop in performance, particularly with structure A27, as the greater overlap of the fin rows results in higher heat transfer coefficients at a position with a small fin cross-section than is the case with the other structures.

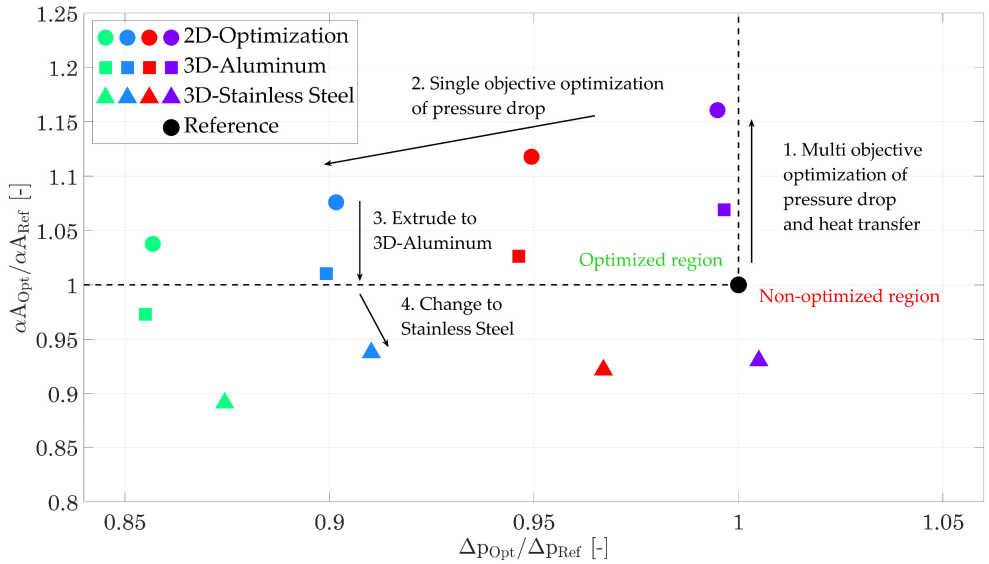

Figure 15. Pareto diagram for the 2D optimization and the 3D-extruded version for aluminum and stainless steel. (Marker Colour: purple: A27, red: B27, blue: C27, green: D27).

An analysis of the pressure loss for stainless steel shows that this increases by 0.2% for variant A27 compared to the 2D variant. For the other variants, a greater decrease can be observed compared to the 2D case, attributed to the smaller temperature differences and, thus, smaller viscosity differences along the fin height and the fluid.

If aluminum is used for finned structures, there is a lower drop in the heat transfer rate compared to the 2D initial structure due to the higher fin efficiency. With the exception of structure D27, a higher heat transfer is achieved for all variants as compared to the reference structure. In the case of aluminum, the areas of the stagnation point can now take advantage of a higher heat transfer and dissipate the heat flux density better.

For the pressure loss, similar behavior can be observed. The calculated relative pressure losses for all structures are close to those of the 2D variants. Due to the higher temperatures and, thus, higher dynamic viscosities in the fluid boundary layer along the fin height, higher fluid friction and pressure losses are present.

3.2. 3D Optimization

The optimizations carried out in advance are limited to 2D shaping, which means that optimizations with regard to fin efficiency and 3D flow control are not taken into account. However, optimizations of the fin efficiency are of great importance for fin materials with lower thermal conductivity, as for stainless steel in this case, as these influence the effectiveness of the heat exchanger accordingly. Furthermore, 3D optimization can reduce unfavorable areas for pressure loss and heat transfer along the fin height. Therefore, a 3D optimization should follow, in which the fin contour also varies along the fin height. The initial structure for the 3D optimization is the reference structure; see Figure 5 with the corresponding boundary conditions.

For the 3D optimization, the multi-objective function is:

$$Z = \min f\left(w_{\mathrm{T_{inner}}}, \mathrm{T_{inner}},\ w_{\Delta p}, \Delta p\right). \tag{22}$$

T_{inner} is the area-weighted average wall temperature along the fins and the base surface ($T_{\mathrm{inner}} = 1/A_{\mathrm{ht}} \sum_i A_{\mathrm{ht,i}} T_{\mathrm{inner,i}}$) and Δp the overall pressure loss of the entire fluid domain. Due to the boundary condition "constant heat flux" at the outer wall, the overall heat flow remains constant. To improve the structure in terms of heat transfer, the inner wall temperature has to be reduced to obtain an improvement in convective heat transfer.

A mesh with very high quality is used for 3D optimization; the minimum orthogonal quality is 0.17, which allows a higher number of optimizations. If the optimization is started with a lower orthogonal quality, negative cell volumes occur prematurely and the calculation is aborted. The meshing is carried out with the "Fluent Meshing" program. Following the optimization, re-meshing is performed again to eliminate the influence of the mesh distortion following the optimization.

A total of four optimization directions are carried out with different weightings of pressure loss and the area-averaged wall temperature; the weightings of the two optimization values are listed in Table 6. A total of 10 iterations with a freeform scale factor of 25 are carried out for each weighting pair. If the orthogonal quality falls below 0.12, the mesh is optimized using Fluent's "mesh improve" function, which raises the minimum orthogonal quality again.

Table 6. Weight pairs for the 3D optimization.

Structure	w_{Tinner}	w_{dp}
0dp1ht	0.845	0.155
04dp06ht	0.819	0.181
06dp04ht	0.765	0.235
1dp0ht	0.723	0.277

Figure 16 shows the trend of the mean internal wall temperature, the product of heat transfer and surface area, as well as the pressure loss and its relative change for structure 0dp1ht.

The curves show that the average inner wall temperature decreases with increasing design iteration while the product of the heat transfer coefficient and surface area increases accordingly to a 3% improvement.

The analysis of the pressure loss shows that it increases slightly over the number of iterations to a maximum of 0.15%.

Figure 17 shows the change from the initial structure to the final iteration step. The comparison shows that there are changes to the fin root, fin flank and fin tip compared to the initial structure. There are slight constrictions at the base of the fin in the area of the stagnation point and the detachment area, which increases the flow cross-section in this area and thus reduces the local pressure loss and simultaneously increases the heat transfer, as part of the mass flow is shifted to the lower area of the fins. There are also corresponding constrictions in the area of the fin tip; at these points, areas of the fins that are of secondary

importance for heat transfer are removed, while this benefits the pressure loss due to the larger flow cross-section. At the same time, this benefit of lower pressure loss can now be used to optimize heat transfer at a more effective location. This occurs, for example, in the lower area of the fin flank, where slight thickening occurs compared to the reference case. This leads to higher velocities in this area and thus to higher heat transfer rates. Due to the thickening, the heat-conducting cross-section of the fin also increases, which reduces the average fin temperature. The constrictions in the area of the base of the fin are more pronounced, and the thickening in the lower area of the fin flank is smaller. This leads to larger flow cross-sections and, therefore, lower pressure losses, while the heat transfer is reduced only minimally.

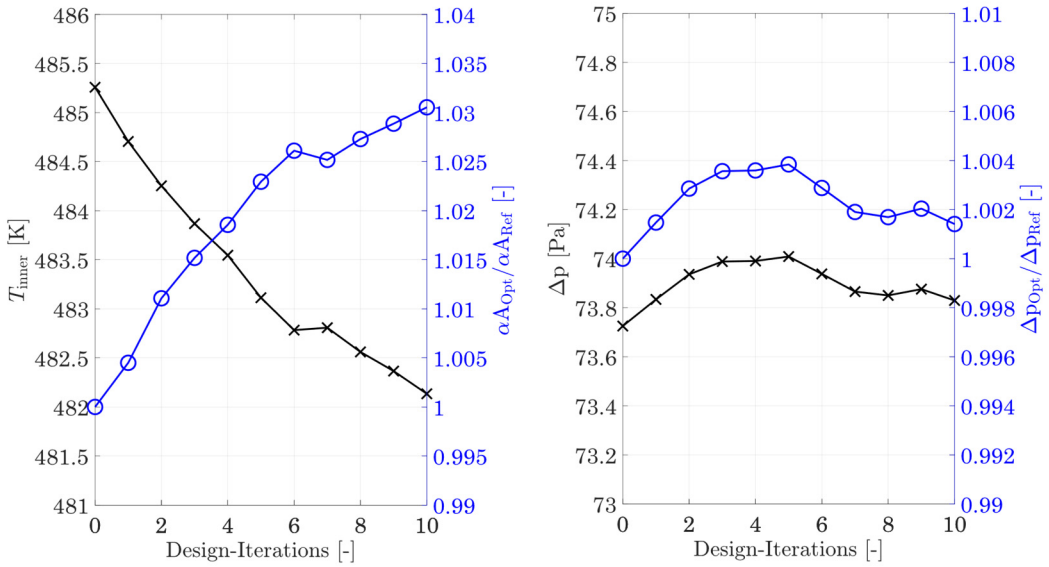

Figure 16. Profile of the inner wall temperature and pressure loss for the 3D optimization 0dp1ht.

The results for the different optimizations depending on the different weights, as well as the different design iterations, are shown in Figure 18. The analysis of the design iterations for 0dp1ht shows that an improvement in heat transfer can be achieved quickly with the first design iterations 1–5, while the improvements are significantly smaller from the 6th iteration onwards. An improvement of the heat transfer at constant pressure loss is thus obviously increasingly difficult, which from an optimization point of view, indicates a possible local optimum.

A similar result is determined for the weight-pair 04dp06ht. For the first seven design iterations, the improvement of the heat transfer is almost equally distributed. For the last three design iterations, the improvement in heat transfer decreases, and the reduction in pressure loss is greater instead than for the first seven iterations. It appears there is also an increasing difficulty in further optimization of the heat transfer. For the structures 06dp04ht and 1dp0ht, with a focus on pressure loss optimization, this trend is not shown, and the improvement for the different design iterations is equally distributed.

The Colburn j-factor and the Fanning f-factor for different Reynolds numbers are shown in Figure 19.

The curve shows that the optimized variants also show a better heat transfer with simultaneously reduced pressure loss than the reference structure at other Reynolds numbers apart from the optimized variant. The relative improvement or reduction continues to match the values at the optimization point with a tolerance of around 10% for all Reynolds numbers investigated.

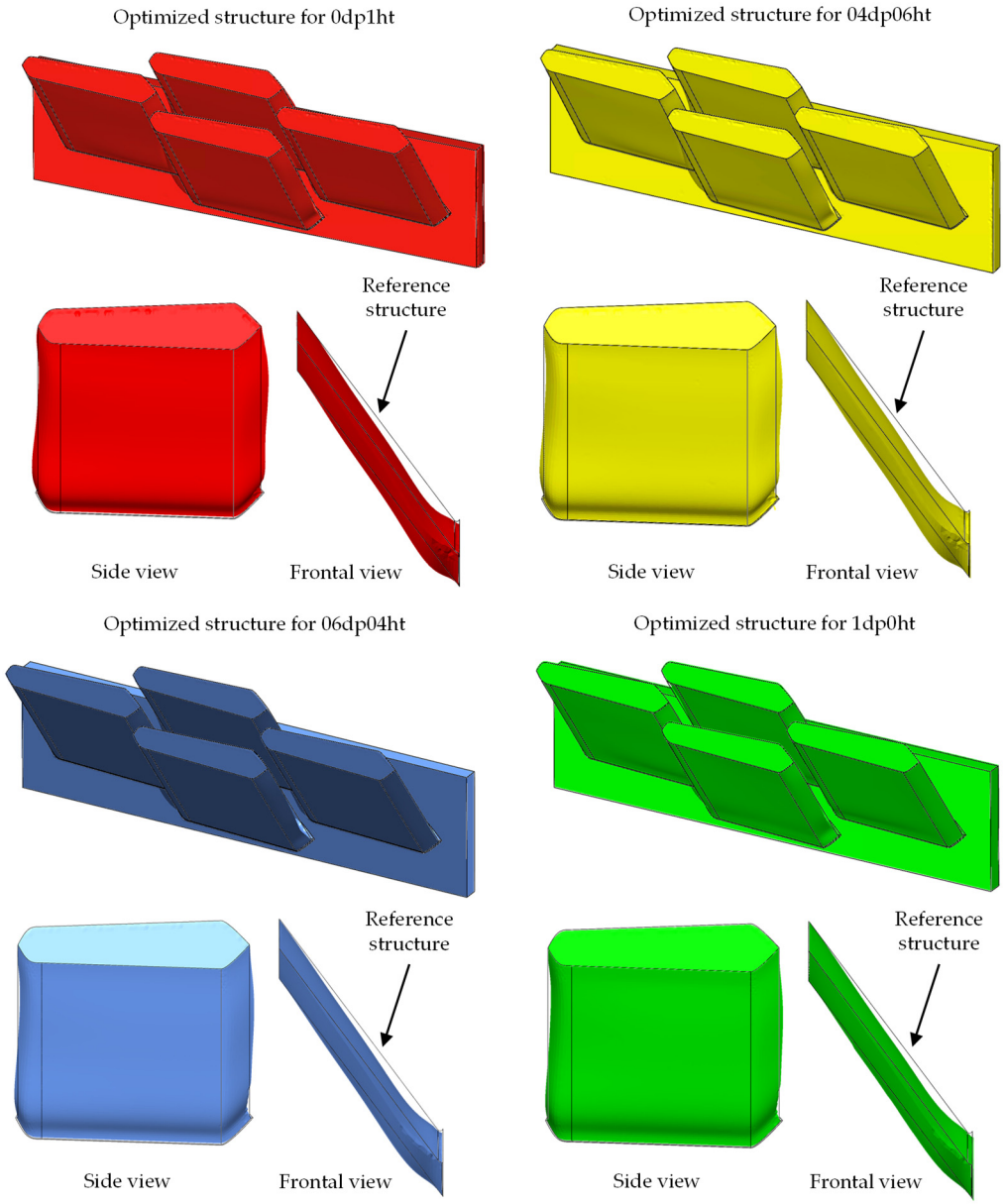

Figure 17. Geometry modifications for the four different weight pairs (indicated by different colours). The fins for the side and frontal view are the ones from the second row.

This results in the following coefficients in Table 7 for Equations (14) and (15) for the Colburn j-factor and the Fanning f-factor, respectively.

Table 7. Coefficients for the Colburn j-factor and Fanning f-factor for the different optimized fins.

Structure	C_j	n_j	C_f	n_f
0dp1ht	0.786	−0.619	12.819	−0.844
04dp06ht	0.784	−0.619	12.411	−0.842
06dp04ht	0.782	−0.622	11.631	−0.838
1dp0ht	0.774	−0.623	11.08	−0.834

Two of these 3D-optimized structures are also examined experimentally in order to investigate the accuracy of the calculation in this optimization test.

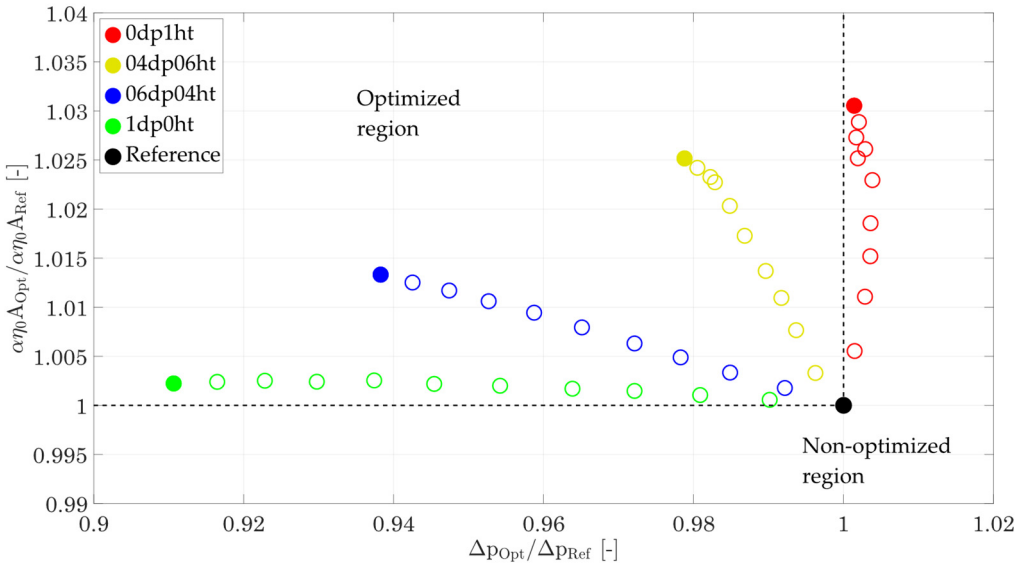

Figure 18. Pareto diagram for the 3D optimization. The hollow symbols represent the different design iterations 1–10, and the filled symbols represent the final geometry.

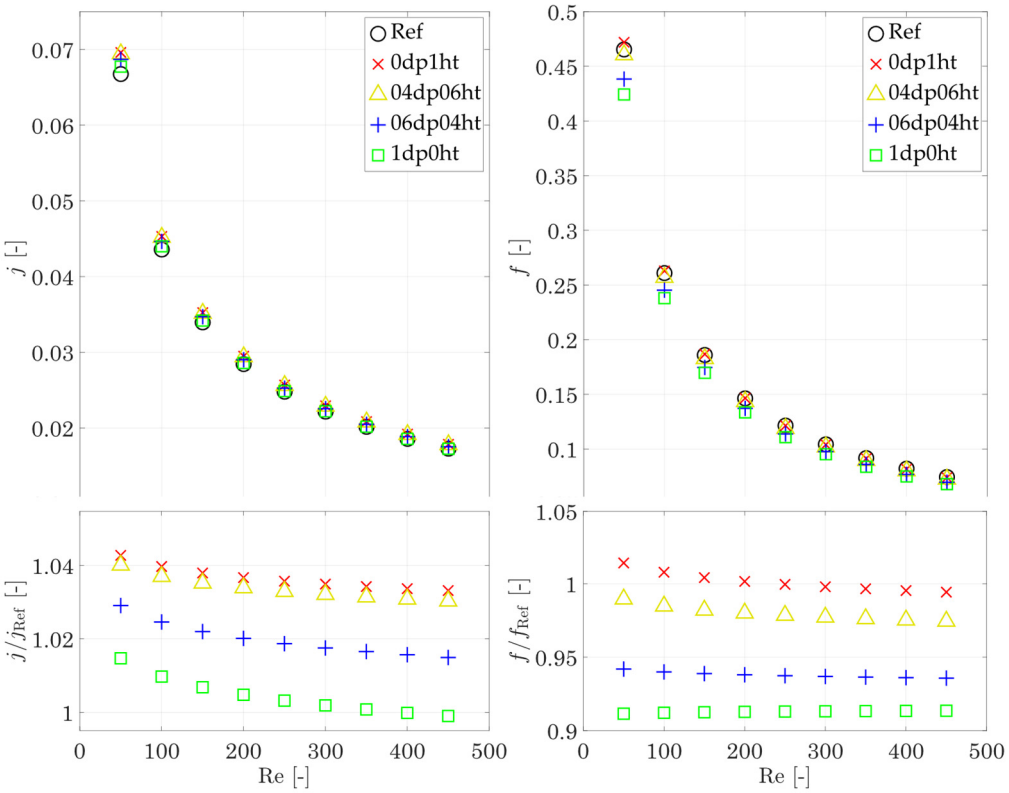

Figure 19. Colburn j-factor, Fanning f-factor and the ratios compared to the reference structure for the different optimizations.

3.3. Experimental Testing

The optimizations made in advance are to be verified by means of experiments. Therefore, two versions with a focus on increased heat transfer (0dp1ht) and reduced pressure loss (1dp0ht) are manufactured. The structure 1dp0ht will also be analyzed in terms of surface roughness and manufacturing accuracy.

The analysis of the surface roughness in Figure 20 yields values of approximately 25 µm on the top side of the fin structures and 63 µm on the bottom side on average.

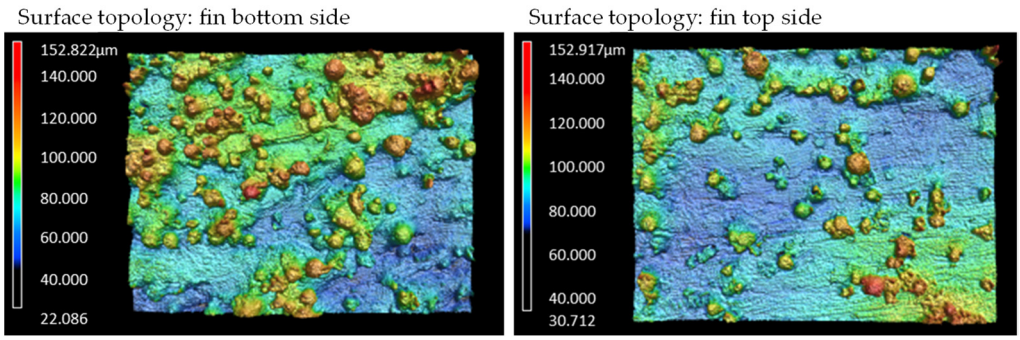

Figure 20. Surface topology of the top and bottom side of the fin.

Due to the small duct dimensions of 380 µm, the roughness leads to a recurring constriction of the flow, which could result in a higher pressure loss.

This is further intensified by the general manufacturing deviation. An X-ray microscope analysis shows that the deviation between the manufactured test object and the CAD model is approximately +20–40 µm in all spatial directions (see Figure 21 for the X-ray image). This leads to smaller channels and distances between the fins and thus to smaller flow cross-sections.

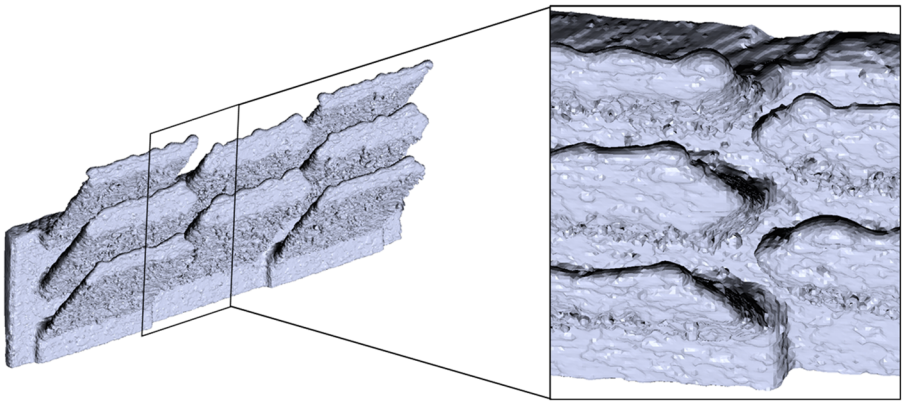

Figure 21. 3D-X-ray image of the structure 1dp0ht.

The smallest channel width between two rows of fins is approximately 350 µm for 0dp1ht and 380 µm for 1dp0ht in the 3D model, when considering the manufacturing accuracies from the 1dp0ht X-ray analysis, this leads to 23% (0dp1ht) and 21% (1dp0ht) smaller distances, resulting in 270 µm (0dp1ht) and 300 µm (1p0ht). This has a direct effect on the flow cross-section and thus on the hydraulic diameter, which ultimately results in higher pressure losses. Using an updated hydraulic diameter with the corrected minimum flow cross-section, a corrected f-factor f_{corr} can be determined by applying Equation (20).

The X-ray analysis also reveals that the predicted missing geometry in Figure 12 is present at the leading and trailing edge of the fins, which influences the heat transfer coefficients, due to the changed stagnation point and the thermal boundary layer in this region.

Figure 22 shows the relative deviation between the experiment and the numerical calculation. For the structure 0dp1ht, the agreement between the experiment and the calculation is between 0.9 and 1.07. This means there is an underestimation of small Reynolds numbers and an overestimation of higher Reynolds numbers. Compared to other investigations of additively manufactured heat exchangers (see introductory chapter), the

agreement between the experiment and the calculation can be described as good to very good. However, the fluctuation compared to the improvement in heat transfer is large, meaning that the theoretical improvements in heat transfer can only be mapped to a limited extent due to manufacturing inaccuracies in the manufacturing process. The analysis of the f-factor initially shows a very large deviation of a factor of ~2.5.

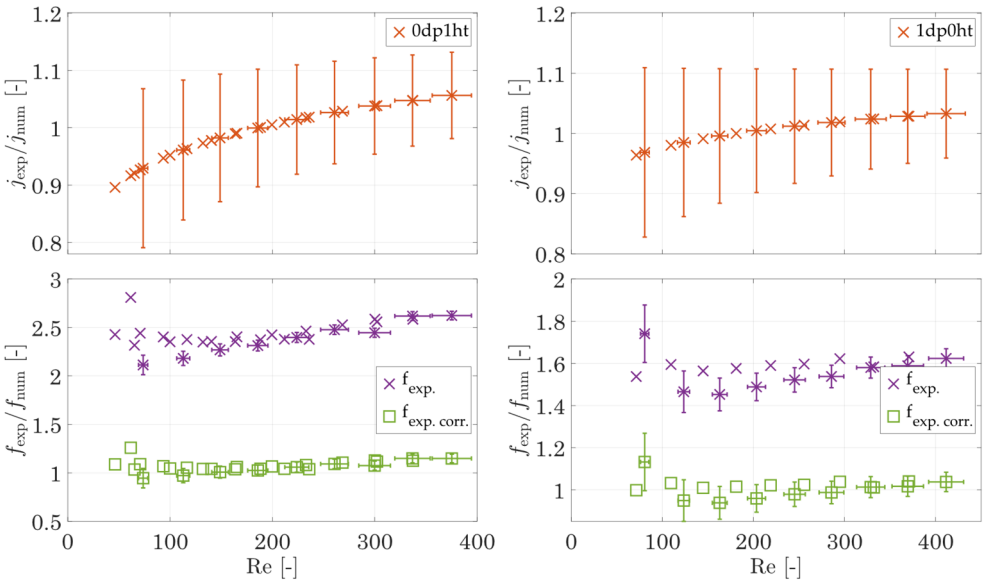

Figure 22. The ratio of experimental and numerical results for the j-factor and the f-factor (**Left**: 0dp1ht. **Right**: 1dp0ht).

The analysis of the j-factor of the structure 1dp0ht shows a significantly better agreement, which ranges between 0.97 and 1.03. As with 0dp1ht, there is a tendency to underestimate small Reynolds numbers and overestimate larger Reynolds numbers. In the experiment, the f-factor is initially overestimated by approximately 1.6.

The uncertainties of the Colburn j-factor and the Fanning f-factor are summarized in Table 8 for both structures. For the Colburn j-factor the uncertainty ranges between 7% for large and 12% for small Reynolds numbers, and for the Fanning f-factor between 4.4–10% for large and small Reynolds numbers. The uncertainty of the Reynolds number is around 5.1–6.1%.

Table 8. Uncertainty range of the Colburn j-factor, the Fanning f-factor and the Reynolds number.

Structure	Δj [%]	Δf [%]	ΔRe [%]
0dp1ht	±7.04–13.27	±4.43–10.07	±5.11–6.12
1dp0ht	±6.88–13.44	±4.43–9.27	±5.11–6.12

If the f-factors of the measurements are corrected for the new flow cross-section due to manufacturing deviations (and not considering possible acceleration due to roughness), the differences between the experimental and numerical values for 0dp1ht and 1dp0ht can be reduced significantly to less than 10% on average.

This also indicates that possible deviations due to the difference between the optimization (three rows of fins) and the fin arrangement in the heat exchanger (~14 rows of fins) are not the main cause of the existing deviations and at most cause small differences.

The causes for the underestimation and overestimation of the j-factors cannot be determined directly. However, it is assumed that the underestimation at low Reynolds numbers is due to possible detachment areas caused by the surface roughness. If the Reynolds number is increased, there is a slight overestimation, which could also be caused by the roughness and the associated increase in turbulence.

The experimental investigations show that although the optimizations made can be reproduced by 3D printing, the limits of manufacturing accuracy are also reached, as the fluctuations of the experiment sometimes exceed the potential for improvement, especially in terms of heat transfer improvement.

4. Discussion

The numerical investigations show that a further increase in heat transfer with a simultaneous reduction in pressure loss is possible in principle using the Adjoint Optimization Method. Performing the optimizations in 2D and subsequently transferring the structure into three dimensions leads to a reduction in performance of 15–20% in the case of materials with low thermal conductivities, such as stainless steel, as the resulting fin efficiency drops to 60–80%. To compensate for this, materials with high thermal conductivity, such as aluminum, must be used. However, the 2D-optimized structures transferred to three dimensions still exhibit significantly reduced pressure losses compared to the reference structure, as strong flow deflections are reduced.

To optimize materials with low thermal conductivity, such as stainless steel, a 3D optimization is therefore carried out directly. Using a multi-objective optimization, a reduction in pressure loss of 9% with a constant heat transfer rate or an increase in heat transfer of 3.5% with a constant pressure loss for stainless steel after 10 design iterations can be achieved, depending on the choice of weighting. The reduction in pressure loss is mainly achieved by reducing flow-unfavorable areas in the area of the fin base. The simultaneous increase in convective heat transfer is achieved by thickening the base of the fin at the fin flank and shifting the leading edge of the fin into the area of higher velocities. This leads to higher fin efficiencies and higher heat transfer coefficients at the stagnation point of the fins close to the fin base.

The resulting correlations for the j- and f-factors based on the coefficients in Table 7 and the Equations (14) and (15) are summarized in Table 9.

Table 9. Correlations for the Colburn j-factor and the Fanning f-factor for different optimizations.

Structure	Colburn j-Factor	Fanning f-Factor
0dp1ht	$j = 0.786\ \mathrm{Re}^{-0.619}$	$f = 12.819\ \mathrm{Re}^{-0.844}$
04dp06ht	$j = 0.784\ \mathrm{Re}^{-0.619}$	$f = 12.411\ \mathrm{Re}^{-0.842}$
06dp04ht	$j = 0.782\ \mathrm{Re}^{-0.622}$	$f = 11.631\ \mathrm{Re}^{-0.838}$
1dp0ht	$j = 0.774\ \mathrm{Re}^{-0.623}$	$f = 11.08\ \mathrm{Re}^{-0.834}$

The subsequent experimental investigation using two structures confirms the mappability of the resulting geometry changes. The analysis of the j-factor generally shows good agreement between the numerical and experimentally determined values. A consideration of the f-factor shows a clear overestimation of the numerical data for both structures. This is attributed to the increasing overlapping fin rows and the manufacturing deviations. These lead to a reduced cross-section area between two rows of fins and thus to a locally increased velocity, which has a negative effect on the pressure loss. This effect is further intensified by the increased roughness on the underside of the fins, as roughness elevations can protrude far into the flow and also reduce the cross-section area. If these manufacturing deviations are taken into account in the calculation of the f-factor, a parallel shift of the experimental f-factor curve can be observed, which leads to good agreement with the numerical data. This behavior can be demonstrated for both structures investigated.

5. Conclusions

This article shows that further improvement in convective heat transfer with a simultaneous reduction in pressure loss is possible using a multi-objective adjoint optimization as compared to a reference structure. For materials with high thermal conductivity, such as aluminum, an optimization can be carried out in 2D and then simply be transferred to

3D in order to achieve an improvement. If, on the other hand, materials with low thermal conductivity (stainless steel or nickel-based alloys) are to be used, improvements in thermal performance cannot be achieved, although there is still a lower pressure loss than in the reference case.

In order to achieve an improvement here, a full 3D optimization must be used. This requires a very high quality for the computational mesh used in order to be able to calculate sufficient design iterations. The evaluation shows that an improvement in convective heat transfer with a simultaneous reduction in pressure loss is also possible here and that a corresponding focus can be placed through the choice of weighting.

The experimental investigations using two optimization directions show that the optimizations made are not only numerical in nature but can also be mapped in terms of production technology and have corresponding effects on heat transfer and pressure loss. However, the experiments also show that the smaller the flow cross-sections, the greater the deviations, particularly in terms of pressure loss. However, by considering these deviations, the agreement in the present cases can be significantly improved.

Finally, correlations for the calculation of the Colburn j-factor and the Fanning f-factor for the 3D adjoint-optimized fin structures are available, which enable a fast prediction in design tools.

Author Contributions: Conceptualization, M.F.; methodology, M.F. and C.N.D.; software, M.F. and C.N.D.; validation, M.F.; formal analysis, M.F. and C.N.D.; investigation, M.F. and C.N.D.; resources, M.F. and S.K.; data curation, M.F.; writing—original draft preparation, M.F.; writing—review and editing, M.F., C.N.D. and S.K.; visualization, M.F.; supervision, S.K.; project administration, M.F. and S.K.; funding acquisition, M.F. and S.K. All authors have read and agreed to the published version of the manuscript.

Funding: This research was funded by the Federal Ministry for Economic Affairs and Climate Action (BMWK) based on a resolution of the German Bundestag and AiF Projekt GmbH, grant number "KK5174901SN0".

Data Availability Statement: The data are not available due to intellectual property.

Acknowledgments: The authors gratefully thank Lauris Richter-Meitze for performing the 3D–X-Ray analysis.

Conflicts of Interest: The authors declare no conflicts of interest.

Nomenclature

$A*$	fin cross-section, mm^2	$n_{j/f}$	Parameter for Equations (14) and (15)
$A_{ht,tot}$	total heat transfer area, m^2	p	pressure, Pa
$A_{ht,fin}$	fin heat transfer area, m^2	P	Fin perimeter, mm
$A_{c,f}$	flow cross-section, m^2	Pr	Prandtl-Number
$C_{j/f}$	Parameter for Equations (14) and (15)	$\dot{Q}$	heat flow, W
c_p	specific isobaric heat capacity, J/kg K	R	Design variable
d_h	hydraulic diameter, mm	L	Lagrange duality
f	Fanning friction factor	Re	Reynolds Number
G	equations of conservation	s	error function
h_{fin}	fin height, m	S	flow variables
j	Colburn j-factor	T	Temperature, K
$kA_{\text{exp/th,i}}$	overall heat transfer coefficient, W/K	u	velocity in flow direction, m/s
L	Lagrange duality	w	weight for cost function
L, l	Length (domain or heat exchanger), m	V	Volume of domain (fluid, wall), m^3
$\dot{m}$	mass flow rate, kg/s	x, y, z	coordinate, m
N_{test}	number of measuring points	Z	cost function
Greek Letters			
α	heat transfer coefficient, W/m^2K	$\eta_{fin/0}$	fin/surface efficiency
Δp	pressure loss, Pa	λ	thermal conductivity, W/mK
$\Delta T_{\log}$	logarithmic temperature difference, K	λ^T	Lagrangian multiplier
ζ	loss coefficient for Equation (19)	μ	dyn. Viscosity, Pa s
		ρ	density, kg/m^3
Subscripts and Superscripts			
a	heat transfer	In	inlet
c	cold	log	logarithmic
con	contraction	m	mean

Dist	Distributor	max	maximum
ex	expansion	out	outlet
exp	experimental	ref	reference structure
f	fin, fluid	th	theoretical
fric	friction	w	wall
H	hot		

References

1. Niknam, S.A.; Mortazavi, M.; Li, D. Additively manufactured heat exchangers: A review on opportunities and challenges. *Int. J. Adv. Manuf. Technol.* **2021**, *112*, 601–618. [CrossRef]
2. Liang, D.; He, G.; Chen, W.; Chen, Y.; Chyu, M.K. Fluid flow and heat transfer performance for micro-lattice structures fabricated by Selective Laser Melting. *Int. J. Therm. Sci.* **2022**, *172*, 107312. [CrossRef]
3. Tang, W.; Zhou, H.; Zeng, Y.; Yan, M.; Jiang, C.; Yang, P.; Li, Q.; Li, Z.; Fu, J.; Huang, Y.; et al. Analysis on the convective heat transfer process and performance evaluation of Triply Periodic Minimal Surface (TPMS) based on Diamond, Gyroid and Iwp. *Int. J. Heat. Mass. Transf.* **2023**, *201*, 123642. [CrossRef]
4. Bacellar, D.; Aute, V.; Huang, Z.; Radermacher, R. Design optimization and validation of high-performance heat exchangers using approximation assisted optimization and additive manufacturing. *Sci. Technol. Built Environ.* **2017**, *23*, 896–911. [CrossRef]
5. Wenterodt, T. *Die Bewertung und Numerische Optimierung von Wärmeübertragern Anhand Einer Energieentwertungszahl*; Technische Universität Hamburg-Harburg: Hamburg, Germany, 2013.
6. Vidya, M.C. Modeling and Adjoint Optimization of Heat Exchanger Geometries. Ph.D. Thesis, University of Twente, Enschede, The Netherlands, 2020. [CrossRef]
7. Wang, C.-Z.; Nagisetty, K.R.; Montanari, F.; Hill, D.C. Application of Adjoint Solver to Optimization of Fin Heat Exchanger. In *Volume 5C: Heat Transfer*; American Society of Mechanical Engineers: Montreal, QC, Canada, 2015; p. V05CT15A020. [CrossRef]
8. Czerwiński, G.; Wołoszyn, J. Optimization of Air Cooling System Using Adjoint Solver Technique. *Energies* **2021**, *14*, 3753. [CrossRef]
9. Kametani, Y.; Fukuda, Y.; Osawa, T.; Hasegawa, Y. A new framework for design and validation of complex heat transfer surfaces based on adjoint optimization and rapid prototyping technologies. *JTST* **2020**, *15*, JTST0016. [CrossRef]
10. Kametani, Y.; Watanabe, S.; Hasegawa, Y. Multi-Objective Adjoint-Based Shape Optimization of Heat Transfer Surfaces in Turbulent Flows with Dns-Rans Hybrid Approach. In *Proceeding of International Heat Transfer Conference 17*; Begellhouse: Cape Town, South Africa, 2023; p. 9. [CrossRef]
11. Kühl, N.; Müller, P.M.; Rung, T. Adjoint Complement to the Universal Momentum Law of the Wall. *Flow. Turbul. Combust.* **2022**, *108*, 329–351. [CrossRef]
12. Li, M.; Wang, J.; Chen, Z.; Qian, X.; Sun, C.; Gan, D.; Xiong, K.; Rao, M.; Chen, C.; Li, X. A Comprehensive Review of Thermal Management in Solid Oxide Fuel Cells: Focus on Burners, Heat Exchangers, and Strategies. *Energies* **2024**, *17*, 1005. [CrossRef]
13. Roetzel, W.; Luo, X.; Chen, D. *Design and Operation of Heat Exchangers and Their Networks*; Elsevier: Amsterdam, The Netherlands, 2020. [CrossRef]
14. Fuchs, M.; Lubos, N.; Kabelac, S. Numerical Calculation of the Irreversible Entropy Production of Additively Manufacturable Off-Set Strip Fin Heat-Transferring Structures. *Entropy* **2023**, *25*, 162. [CrossRef]
15. Fuchs, M.; Kabelac, S. Numerical Calculation of the Irreversible Entropy Production in Heat Transferring Structures. *Chem. Ing. Tech.* **2023**, *95*, 692–700. [CrossRef]
16. Fuchs, M.; Bodemer, J.; Kabelac, S. Experimental investigation of additively manufactured high-temperature heat exchangers. *Int. J. Heat Mass Transf.* **2024**, *218*, 124774. [CrossRef]
17. Ansys Corp. Ansys Fluent. 2021. Available online: https://www.ansys.com/products/fluids/ansys-fluent (accessed on 27 February 2024).
18. Dassault Systemes Deutschland GmbH. SolidWorks. 2020. Available online: https://www.solidworks.com/de (accessed on 27 February 2024).
19. Ansys Corp. Ansys DesignModeler. 2021. Available online: https://www.ansys.com/products/ansys-workbench#tab1-2 (accessed on 27 February 2024).
20. Menter, F.R. Two-equation eddy-viscosity turbulence models for engineering applications. *AIAA J.* **1994**, *32*, 1598–1605. [CrossRef]
21. Giles, M.B.; Pierce, N.A. An Introduction to the Adjoint Approach to Design. *Flow Turbul. Combust.* **2000**, *65*, 393–415. [CrossRef]
22. Gauger, N.R. Adjoint Approaches In Aerodynamic Shape Optimization And Mdo Context. In Proceedings of the ECCOMAS CFD 2006: Proceedings of the European Conference on Computational Fluid Dynamics, Egmond aan Zee, The Netherlands, 5–8 September 2006.
23. Ahmad, T.; Plee, S.L.; Myers, J.P. ANSYS Fluent Theory Guide. *Release* **2013**, *15*, 814.
24. Jameson, A. *Aerodynamic Shape Optimization Using the Adjoint Method; Lectures at the Von Karman Institute: Brussels, Belgium, 2003.*
25. Lyu, Z.; Kenway, G.K.; Paige, C.; Martins, J.R.R.A. Automatic Differentiation Adjoint of the Reynolds-Averaged Navier-Stokes Equations with a Turbulence Model. In Proceedings of the 21st AIAA Computational Fluid Dynamics Conference, San Diego, CA, USA, 24–27 June 2013; American Institute of Aeronautics and Astronautics: San Diego, CA, USA, 2013. [CrossRef]
26. Kavvadias, I.S.; Papoutsis-Kiachagias, E.M.; Dimitrakopoulos, G.; Giannakoglou, K.C. The continuous adjoint approach to the *k*–ω *SST* turbulence model with applications in shape optimization. *Eng. Optim.* **2015**, *47*, 1523–1542. [CrossRef]

27. Stephan, P.; Kabelac, S.; Kind, M.; Mewes, D.; Schaber, K.; Wetzel, T. (Eds.) *VDI-Wärmeatlas: Fachlicher Träger VDI-Gesellschaft Verfahrenstechnik und Chemieingenieurwesen*; Springer Reference Technik; Springer: Berlin/Heidelberg, Germany, 2019. [CrossRef]
28. Baker, T.J. *Fluent User's Guide*; ANSYS, Inc.: Canonsburg, PA, USA, 2023.
29. Bernhard, F. (Ed.) *Handbuch der Technischen Temperaturmessung*; Springer: Berlin/Heidelberg, Germany, 2014. [CrossRef]
30. Joint Committee for Guides in Metrology. Evaluation of Measurement Data—Guide to the Expression of Uncertainty in Measurement. 2008. Available online: https://www.iso.org/sites/JCGM/GUM/JCGM100/C045315e-html/C045315e.html?csnumber=50461 (accessed on 27 February 2024).
31. Fuchs, M.; Luo, X.; Kabelac, S. Influence of axial heat conduction in solid walls and fins on the overall thermal performance of an additively manufactured high-temperature heat exchanger. *Appl. Therm. Eng.* **2022**, *212*, 118566. [CrossRef]
32. Kays, W.M. Loss Coefficients for Abrupt Changes in Flow Cross Section with Low Reynolds Number Flow in Single and Multiple-Tube Systems. *J. Fluids Eng.* **1950**, *72*, 1067–1074. [CrossRef]
33. Lange, F.; Hein, C.; Li, G.; Emmelmann, C. Numerical optimization of active heat sinks considering restrictions of selective laser melting. In Proceedings of the 2018 COMSOL Conference, Lausanne, Switzerland, 22–24 October 2018; p. 7.